hydrogen

MDPI

Article

Study of Activity and Super-Capacitance Exhibited by Bifunctional Raney 2.0 Catalyst for Alkaline Water-Splitting Electrolysis

William J. F. Gannon and Charles W. Dunnill *

Energy Safety Research Institute, Swansea University Bay Campus, Fabian Way, Swansea SA1 8EN, UK; w.j.f.gannon@swansea.ac.uk

* Correspondence: c.dunnill@swansea.ac.uk

Abstract: Low-cost, high-performance coatings for hydrogen production via electrolytic water-splitting are of great importance for de-carbonising energy. In this study the Raney2.0 coating was analysed using various electrochemical techniques to assess its absolute performance, and it was confirmed to have an extremely low overpotential for hydrogen evolution of just 28 mV at 10 mA/cm^2. It was also confirmed to be an acceptable catalyst for oxygen evolution, making it the highest performing simple bifunctional electrocatalyst known. The coating exhibits an extremely high capacitance of up to 1.7 F/cm^2, as well as being able to store 0.61 J/cm^2 in the form of temporary hydride deposits. A new technique is presented that performs a best-fit of a transient simulation of an equivalent circuit containing a constant phase element to cyclic voltammetry measurements. From this the roughness factor of the coating was calculated to be approximately 40,000, which is the highest figure ever reported for this type of material. The coating is therefore an extremely useful improved bifunctional coating for the continued roll-out of alkaline electrolysis for large-scale renewable energy capture via hydrogen production.

Keywords: alkaline; electrolysis; water-splitting; hydrogen production; constant phase element

Citation: Gannon, W.J.F.; Dunnill, C.W. Study of Activity and Super-Capacitance Exhibited by Bifunctional Raney 2.0 Catalyst for Alkaline Water-Splitting Electrolysis. *Hydrogen* **2020**, 2, 1–17. https://doi.org/10.3390/hydrogen2010001

Received: 23 September 2020
Accepted: 21 December 2020
Published: 30 December 2020

1. Introduction

Alkaline water-splitting electrolysis is a mature technology, with a long track-record of producing hydrogen for industrial applications going back over many decades. Despite this, its use for energy capture and storage applications has been severely limited by its high cost. Hydrogen is inevitably cheaper to produce by the reforming of low-cost hydrocarbons such as methane, rather than via the splitting of a thermodynamically stable compound such as water. However, as a result of the inexorable and readily apparent consequences of global warming, the case for modern societies with decarbonised energy systems continues to grow. This case has been strengthened further by the coronavirus lockdown of 2020, which within weeks led to drastic reductions in the levels of carbon-related air pollution normally experienced by many of the world's urban inhabitants.

An example of such decarbonisation is the commitment made by the city of Copenhagen to achieve carbon neutrality by 2025, largely by further extension of existing initiatives. Currently, 36% of all journeys within the city are made by bicycle, and there are plans to bring 85% of the population within 600 m of a subway station. However, the bulk of the reductions will be achieved by alternative methods for the generation of heat and electricity, particularly the concept of combined heat and power. Thus, the city boasts not just the world's largest district heating system, but also a district cooling system based on seawater that, compared with conventional air-conditioning, results in a reduction in carbon emissions of 70% (sources: https://www.theguardian.com/environment/2013/apr/12/copenhagen-push-carbon-neutral-2025, https://www.weforum.org/agenda/2019/05/the-copenhagen-effect-how-europe-can-become-heat-efficient/).

Amongst the buildings in Copenhagen that already benefit from such low-carbon cooling are data centres, which globally have a carbon footprint that is of great concern. The combined carbon output of all the world's communication technology is already on a par with that of the aviation industry [1], but unlike the aviation industry, its emissions are set to triple in the next 10 years [2]. Within that, the electricity consumption of data centres and the associated wired networks to connect them is predicted to quintuple by 2030, accounting for nearly 70% of total Information and Communications Technology (ICT) consumption [2]. With energy usage doubling every four years, by 2040 if unchecked the consumption would be equal to that of the US (source: https://www.computerworld.com/article/3431148).

Meanwhile, conventional forms of fossil-derived energy have experienced reduced levels of demand. At the peak of the lockdown the price of aviation fuel fell to 80% below pre-2020 levels at just $16 per barrel (source: https://www.iata.org/en/publications/economics/fuel-monitor/ viewed using Wayback Machine https://web.archive.org for 11 May 2020). Three weeks earlier, as a result of contractual obligations by traders to buy oil even though they had nowhere to store it, the benchmark price of US crude oil fell to minus $37 a barrel. Although in the short term this may make it harder for renewable energy to compete on economic terms with legacy generation, in the longer term it highlights the decreasing return on investment available within the oil and gas sector.

If water-splitting electrolysis is to be competitive, efficiency must be increased and costs reduced, and to this end many technologies and materials have been investigated [3–5]. However, it is often the case that increases in efficiency have only been achieved by large increases in cost. This particularly applies to acidic PEM electrolysis, which has remained stubbornly dependent on noble-metal catalysts, particularly for oxygen evolution [6]. Not only does this raise cost, but the scarcity of such metals means that no such technology could ever be scaled. High temperature electrolysis similarly trades electrical efficiency against formidable challenges regarding choice of materials and system longevity. This therefore leaves alkaline electrolysis as the technology still most likely to make up the bulk of future capacity. Meanwhile, if the cost of renewable generation continues to halve every few years, (source: https://www.gov.uk/government/news/offshore-wind-energy-revolution-to-provide-a-third-of-all-uk-electricity-by-2030) the economic case for high efficiency electrolysis could disappear faster than it can be developed.

This brings older technologies back to the fore, and there are few more venerable than Raney nickel. The material was invented in 1926 by American engineer Murray Raney, when seeking an improved method for the hydrogenation of vegetable oils, and is created by dissolving nickel in molten aluminium. Zinc or chromium is then added whilst quenching to produce an alloy, which subsequently undergoes a process called 'activation'. This refers specifically to the reaction of the alloy with sodium hydroxide:

$$M_xAl(s) + OH^- + 2\,H_2O \longrightarrow M_x(s) + Al(OH)_3{}^- + H_2(g) \quad (1)$$

which selectively leaches out the more reactive alloying components, such as Al, to leave just the nickel behind. This creates a sponge-like material, the catalytic properties of which are based not just on its very much increased surface area, but also on nickel's ability to adsorb hydrogen. Of all the first-row transition elements, nickel adheres most closely to Sabatier's Principle, which states:

> the best catalysts should bind atoms and molecules with an intermediate strength: not too weakly in order to be able to activate the reactants, and not too strongly to be able to desorb the products [7]

This is equivalent to stating that the optimum binding energy occurs close to the thermoneutral state, i.e., where $\Delta G = 0$ [8]. At this balance point, the entropy change to and from hydrogen gas is equalised by the enthalpy of adsorption, and hydrogen is thus able to adsorb and desorb at the fastest possible rate. This balance point is exemplified by platinum, which consequently has the second highest exchange current density of any known material. Once incorporated as platinum black, a form with a larger surface area,

its ability to adsorb and desorb hydrogen, and thus resist changes in potential, is precisely what makes it a key component of the ultimate reference electrode. It is also why platinum appears close to the top of volcano plots for hydrogen evolution activity [9]. However, in the absence of abundant supplies of platinum, nickel constitutes a far more practical choice.

The activation of Raney nickel relies on the amphoteric properties of aluminium hydroxide. This means that even though it is almost completely insoluble in water, it is able to dissolve in strong sodium hydroxide by producing sodium aluminate:

$$Al(OH)_3 + NaOH \longrightarrow Na^+[Al(OH)_4]^- \quad (2)$$

Thus the hydroxide has reacted with another hydroxide, as if it were an acid. Less concentrated NaOH will result in the precipitation of $Al(OH)_3$, thus blocking the pores and reducing the surface area of the catalyst. By contrast, decreasing the temperature of the solute slows the reaction down, and tends to increase the surface area [10]. An alternative employed by Schiller et al. with Raney nickel deposited by vacuum plasma spraying was 30 wt% KOH at 80 °C. However, the precipitation of aluminium hydroxide still had to be avoided by the inclusion of 10 wt% K-Na-tartrate-tetrahydrate [11].

Alloying is not the only method by which Raney nickel can be produced, and electrodeposition methods have been investigated commercially since the 1950's [12], and in academia since the 1980's [12–15], in addition to other methods such as pressed powders and plasma spraying [16,17]. Although typically investigated for hydrogen evolution [18–25], as well as in combination with non-abundant compounds [26–28], the coating is also known to perform well for oxygen evolution [29,30].

With electrodeposited Raney nickel, the aluminium is exchanged for zinc, but is otherwise completely analogous. The deposition of zinc not just with nickel, but with many ferrous metals, is regarded as an example of Anomalous Co-Deposition (ACD). The anomaly is based on the observation that the less noble metal can be deposited preferentially, and at a higher percentage than is available in the electrolyte [31]. Several theories have been proposed to explain this anomaly, although without any conclusive success [32]. It is known that a lower deposition current density leads to a higher mass fraction of deposited zinc, and thus after activation the potential for a higher surface area of the finished coating. For example, at a density of 10 mA cm^{-2} the proportion of zinc was measured as 93 wt% [32]. Despite this, deposits which are 50 wt% zinc are thought to be the most effective for electrolysis [19], therefore it is expected that a higher current density will produce the best results.

It is known that pure, polished nickel electrodes are vulnerable to a decrease in activity of up to 400 mV when used for alkaline hydrogen evolution, which has been attributed to hydride formation [33]. It is also known that nickel is more likely to form hydrides in NaOH than KOH [34], as well as at high current density and strong electrolyte [35]. However, this effect was not observed with aluminium-based Raney nickel until the fraction of aluminium fell to very low levels [36]. This loss of Al/Zn is driven by the sort of reduced duty-cycle which is typical of renewable energy, with each current interruption causing the cathode to become briefly anodic, thus leaching out the less noble components. The Zn is therefore able to protect the nickel cathode from current interruption corrosion by acting sacrificially. This finding has been confirmed over long-term intermittent experiments on Raney nickel electrodes, where it was observed that Zn was selectively removed from the cathode, but the levels of nickel remained unaffected [37].

Here we investigate the remarkable properties of the 'Raney 2.0' variant of the Raney nickel coating, as deposited on plain 316-grade stainless steel, and show that it has an overpotential for hydrogen evolution of just 28 mV in 1 M KOH, making it one of the highest performing electrocatalysts yet reported. In combination with its modest overpotential for oxygen evolution, this makes it one of the highest performing bifunctional electrocatalysts reported, and certainly the simplest. We show that this activity can be related to its high capacitance and surface area, and also show that a novel technique for the fitting of a transient simulation of an RQ network produced an extremely convincing match to the

measured CV waveforms, thus providing a useful theoretical basis for all high surface area research.

2. Materials and Methods

All procedures were conducted in standard laboratory 100 mL beakers. Such beakers are large enough to accommodate up to two 4 cm × 4 cm paddle-shaped 316-grade stainless-steel (316SS) electrodes, as shown in Figure 1a. All chemicals were standard reagent grade. For Raney1 the counter-electrode was made from a graphite rod. For Raney2 the counter-electrode was made from 316SS, which was partially consumed during the deposition, thereby progressively altering the composition of the coating. The typical appearance of the Raney2 coating, and the three-electrode cell into which it was assembled, were as shown in Figure 1b.

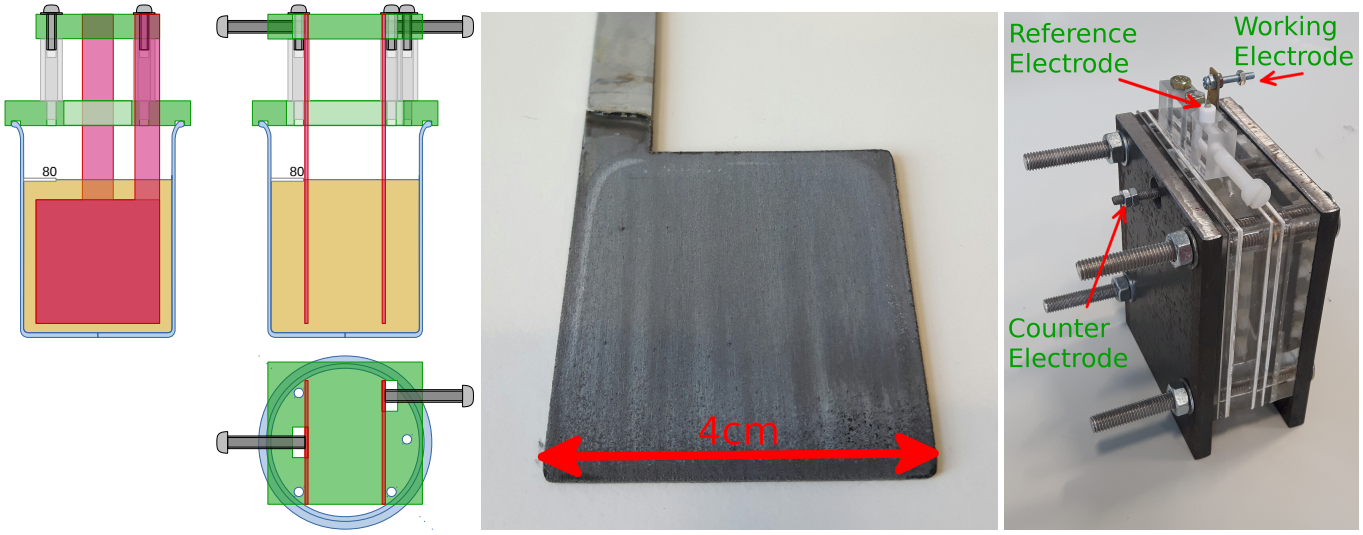

(**a**) (**b**) (**c**)

Figure 1. (**a**) Mechanical drawing of the electrodeposition chamber for Raney2, which employed a 316SS counter-electrode. The chamber was constructed using laser cut acrylic components, plus a standard 100 mL laboratory beaker. (**b**) Typical appearance of the Raney2 coating. (**c**) As assembled into a three-electrode cell.

Electrodeposition: The 4 cm × 4 cm 316SS electrode was degreased in hot 25 wt% NaOH for 1 min, then submerged in 18 wt% HCl for 1 min at room temperature, before being placed in 70 wt% H_2SO_4 for 3 min at an anodic current of 108 mA m^{-2}. The electrode was then placed in a nickel strike solution consisting of 240 g L^{-1} $NiCl_2 \cdot 6\,H_2O$ and 120 mL L^{-1} HCl for 5 min at a cathodic current of −26.8 mA cm^{-2}. Between each step the electrode was rinsed with deionised water, and the air-exposure time minimised. At this point the electrode was covered in a thin, adherent coating of nickel that was able to act as a base for any subsequent functional coating [20]. The electrode was then immersed in a modified Watt's Bath consisting of 330 g L^{-1} $NiSO_4 \cdot 6\,H_2O$, 45 g L^{-1} $NiCl_2 \cdot 6\,H_2O$, 37 g L^{-1} H_3BO_3 and 20 g L^{-1} $ZnCl_2$ at 50 °C for 60 min at a cathodic current of −50 mA cm^{-2}. Lastly the coating was activated by immersion in 6 M NaOH at 50 °C for 48 h.

Potentiostat: All electrochemical experiments were performed on an Ivium n-Stat potentiostat. The electrolyte was 0.5 M NaOH, and the reference electrode was a commercial Ag/AgCl device containing 3 M KCl, which was routinely calibrated against a standard calomel electrode. CV was performed within a 100 mV range around OCP at rates of 10 mV s^{-1} or less. The potential was held for 10 s between changes of direction to allow diffusion gradients within the electrolyte to disperse. EIS was performed at frequencies below 10 kHz around OCP, starting at low frequency. Method: impedance; technique: constant E; amplitude: between 10 mV and 100 mV. The electrode was pretreated for 120 s at OCP to reduce initial transient currents. All EIS results were analysed within the

IviumSoft software package, wherein RCR and RQ equivalent circuits were fitted to the results (where Q is the symbol that represents a CPE).

Equivalent Capacitance: According to Brug et al. the double-layer capacitance for the series connection of a resistor and a constant-phase element can be calculated using:

$$C_{dl} = \left[Q_0 R_s^{(1-n)}\right]^{1/n} \tag{3}$$

where R_s, Q_0 and n are the best-fit parameters of an RQ network to either the EIS or CV results [38,39]. It is worth noting that in the Brug paper Q_0 is referred to as Q^{-1}, and n is referred to as $(1-\alpha)$. Q_0 can be expressed in units of $s^n\ \Omega^{-1}$ and R_s in Ω, or as an area pseudo-capacitance $s^n\ \Omega^{-1}\,\mathrm{cm}^{-2}$ in which case R_s must be in $\Omega\,\mathrm{cm}^2$. From this the roughness factor can be calculated using:

$$RF = C_{dl}/C_s \tag{4}$$

where C_s is the capacitance of a completely smooth surface, which is known to be 40 µF cm^{-2} in alkaline conditions [40].

RQ Transient Best-fit: As a function of time, the voltage across a CPE is given by a convolution integral:

$$V_{CPE}(t) = \frac{1}{Q_0\Gamma(n)}\int_0^t (t-u)^{n-1} i(u)du \tag{5}$$

where Q_0 is the magnitude of the CPE (or its 'pseudo-capacitance'), n is the phase of the CPE, and $\Gamma(\alpha)$ is the gamma function [41]. For cyclic voltammetry, where it is the voltage that is controlled and the current that is measured, solving this involves expressing the electrical network as a differential equation.

For example, for the basic RC network shown in Figure 2 the equation can be expressed as:

$$V_{Total} = \frac{dq}{dt}R + \frac{q}{C} = \frac{dq}{dt}R + V_C \tag{6}$$

where q is electrical charge, such that $i = dq/dt$, and q/C is equal to the voltage on the capacitor V_C. The Euler method can be used to approximate a solution to this equation, based on the first-order simplification that:

$$q_{n+1} = q_n + h\frac{dq}{dt} \tag{7}$$

where h is the step size in time. Replacing the capacitor by a CPE, and therefore V_C by V_{CPE}, produces:

$$q_{n+1} = q_n + h\left(\frac{V_{Total} - V_{CPE}}{R}\right) \tag{8}$$

This iterative scheme can be converted into a computer program, permitting the simulation of the response of the network to any arbitrary voltage waveform (see SI of Reference [42]).

If the values R, Q_0 and n are taken to be the axes of a three-dimensional solution space, then standard gradient descent techniques can be employed to find the position of the best-fit, i.e., the position that minimises a suitable cost-function, for example one defined as the square of the difference between the measured and simulated waveforms.

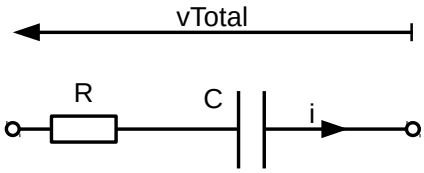

Figure 2. RC Network.

3. Results

3.1. Raney1

The Raney1 coating is deposited using a graphite counter electrode, which does not dissolve, and therefore does not alter the make-up of the coating. It therefore constitutes the standard Raney nickel coating. The typical EIS results for a Raney1 nickel coated 316SS electrode were as shown in Figure 3a. The Figure shows Nyquist plots taken at 3 different values of signal amplitude. Consistent results were produced until the signal amplitude reached about 100 mV. Above this amplitude the course of the plot deviated, which suggests that the electrochemical system was being taken out of its linear zone.

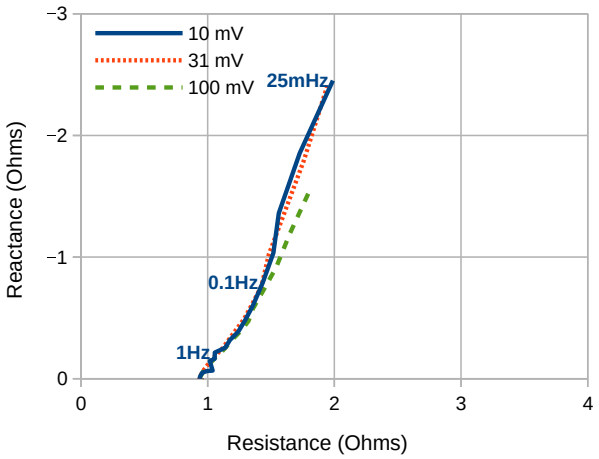

(**a**) Nyquist plots

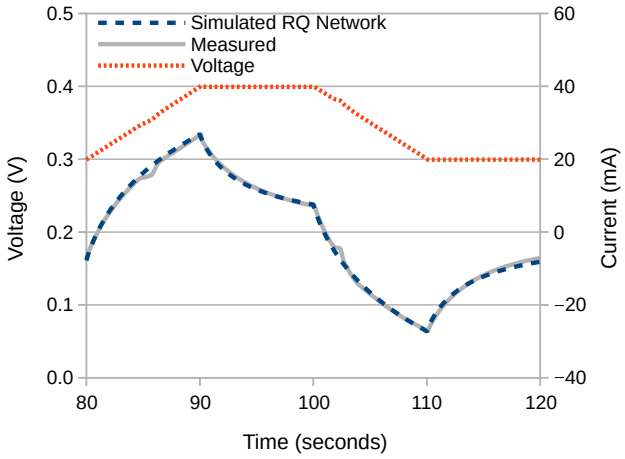

(**b**) CV waveforms

Figure 3. Electrical results for a Raney1 coated 316SS electrode. (**a**) EIS measurements at three different signal amplitudes. Frequency range: 25 mHz to 10 kHz. (**b**) CV waveform recorded at 10 mV s^{-1}. The simulation of the best-fit RQ network has been overlaid.

In all of the traces, the double-layer capacitance of the electrode produced constant-phase behaviour below approximately 1 Hz, in series with a constant ohmic resistance of 0.95 Ω, which for an electrode with an exposed area of 3 cm × 3 cm equates to 8.55 Ω cm^2. The proposed electrical equivalent circuit was therefore a series RQ network, with the best-fit parameters generated by Iviumsoft as presented in the top three rows of Table 1.

The table includes an equivalent capacitance, calculated using Equation (3), which shows that the corresponding double-layer capacitance was about 166 mF cm^{-2}, which equates to a roughness factor of 4150. The higher value of 255 mF cm^{-2} was measured at the highest EIS amplitude, and should be treated with caution.

The CV waveform for the same electrode measured at 10 mV s^{-1} was as presented in Figure 3b. The figure shows that the double-layer capacitance was too high to achieve a stable current value within the time frame available, which made it difficult to extract a straightforward value for the capacitance. As discussed in a previous published work, although it is tempting to fit an RC network to the waveform, it does not have the correct shape. This is because, as is seen for electrodes with lower capacitance, the waveform asymptotes towards a slope. Neither is it possible to fit an RCR network to the waveform, since this produces a misleadingly high value for the capacitance. This is a result of the

constant-phase behaviour of the double-layer capacitance, which not only produces the asymptotic slope, but also alters the curvature of the waveform so that it appears to have a larger time-constant [42].

Table 1. Best-fit parameter values for an RQ network to the EIS and CV results in Figure 3. The error values (if known) are listed in brackets. The equivalent double-layer capacitance C_{dl} has been calculated using Equation (3), and the roughness factor RF using Equation (4).

Trace	R_s	Q_0	n	C_{dl}	RF
	Ω cm^2	s^n Ω^{-1} cm^{-2}		mF cm^{-2}	
EIS at 10 mV	8.57 (0.8%)	0.148 (2.5%)	0.68 (1.9%)	166	4150
EIS at 31 mV	8.52 (0.7%)	0.149 (2.2%)	0.68 (1.6%)	167	4180
EIS at 100 mV	8.47 (0.7%)	0.188 (2.3%)	0.60 (1.9%)	255	6370
CV at 10 mV s^{-1}	9.45	0.206	0.72	266	6650

Therefore the waveform was fitted to an RQ network using the RQ Transient Best-fit method, with the simulation of that network as shown by the dashed blue line in Figure 3b. The best-fit parameters for this network are as shown in the bottom row of Table 1, and produce a convincing match to the measured waveform. To the knowledge of the author, this is the first time that such a technique has been presented in the literature. The CV results therefore suggest a value for the double-layer capacitance of 266 mF cm^{-2}, which equates to a roughness factor of 6650. Some possible explanations for the disparity between the capacitance suggested by EIS and CV will be discussed later.

3.2. *Raney2*

The Raney2 coating was deposited using a 316-grade stainless-steel counter electrode, which partially dissolved during the deposition, and therefore progressively altered the make-up of the coating. It therefore constitutes a version of the coating which has been chemically and morphologically altered by the dissolving stainless-steel [37]. The electrical performance of the Raney2 coating for hydrogen and oxygen evolution was as shown in Figure 4, with the resultant Tafel slopes and overpotentials at 10 mA cm^{-2} as presented in Table 2. The electrode had previously been aged by hydrogen evolution at −70 mA cm^{-2} for 42 h.

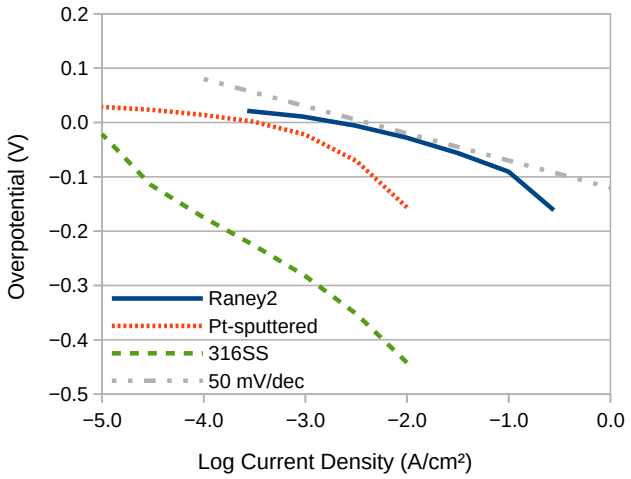

(**a**) Tafel plot for HER

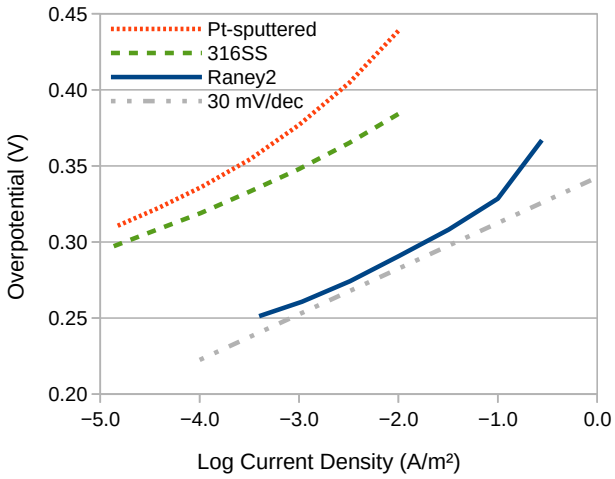

(**b**) Tafel plot for OER

Figure 4. Electrical performance of Raney2-coated 316SS for both HER and OER. Electrolyte: 1 M KOH.

Table 2. Tafel slopes, overpotentials and overall water-splitting voltage for coating Raney2 in 1 M KOH at laboratory temperature, as presented in Figure 4.

Coating	Reaction	Current Density	Tafel Slope	Over-Potential	Voltage
		mA cm^{-2}	mV dec^{-1}	mV	V
Raney2	HER	10	50	28	
Raney2	HER	100	111	91	
Raney2	OER	10	34	291	
Raney2	OER	100	62	328	
Raney2	Both	10	84	320	1.55
Raney2	Both	100	173	419	1.65

The figures show that the performance of the uncoated 316SS for hydrogen evolution was poor, with an overpotential at 10 mA cm^{-2} of nearly 0.45 V. Sputter coating with Pt reduced this overpotential by nearly 0.3 V, which is to be expected since Pt is an excellent hydrogen evolution catalyst. However, with its higher surface area, the Raney2 coating was able to outperform the Pt-coated electrode, achieving a remarkably low overpotential of just 28 mV at the most widely reported benchmark figure of 10 mA cm^{-2}. In fact, the overpotential was still below 100 mV at 100 mA cm^{-2}.

For oxygen evolution, the uncoated 316SS performed well, as has been previously reported [37,43]. It even outperformed the Pt-coated electrode, which underlines how specific Pt is to hydrogen evolution, and why it is not generally used as an OER catalyst [40,44]. In addition, Pt is unstable, and known to dissolve under conditions of alkaline OER [45]. With the Raney2 coating, the overpotential was reduced by 0.1 V, which equates to an increase in current density of more than three orders of magnitude.

It should be noted that these current densities are reported relative to the geometric surface area of the electrode, which places the Pt electrode at a considerable disadvantage. This is fair, because it is much more scalable to generate high area nickel than high area platinum. In fact, it is anticipated that the activity of the Raney2 coating relative to its electrochemical surface area is little different to that of the uncoated electrode, simply because they are both comprised chiefly of nickel and iron. From the horizontal shifts in Figure 4a it can therefore be surmised that Pt is approximately $10^{2.5}$ times more active for HER than 316SS given equal surface areas. However, the Raney2 coating presents approximately 10^4 more effective surface area for HER, and 10^3 for OER, which affords it greater performance.

To further assess the surface area of the Raney2 coating, cyclic voltammograms were recorded for three different voltage sweep rates around OCP, as shown in Figure 5a. These show that the coating has a very high level of capacitance, and the waveforms did not come close to achieving a steady value within the 100 mV window.

Therefore, the voltammograms were rearranged as waveform segments, as shown in Figure 5b. These segments were then suitable for use with the *RQ Transient Best-fit* method, which produced the results presented in Table 3. To aid comparison, the transient simulation results of the three RQ networks have been underlaid under the measurement data in Figure 5b, and produce a convincing level of agreement.

Table 3. Best-fit RQ network parameter values to the cyclic voltammetry waveforms in Figure 5b.

Ramp Rate	R_s	Q_0	n	C_{dl}	RF
mV s^{-1}	Ω cm^2	s^n Ω^{-1} cm^{-2}		F cm^{-2}	
10	9.41	0.811	0.67	2.21	55,170
6.7	9.61	0.784	0.71	1.80	45,000
3.3	9.84	0.762	0.72	1.70	42,490
Average	9.62	0.786	0.70	1.89	47,150

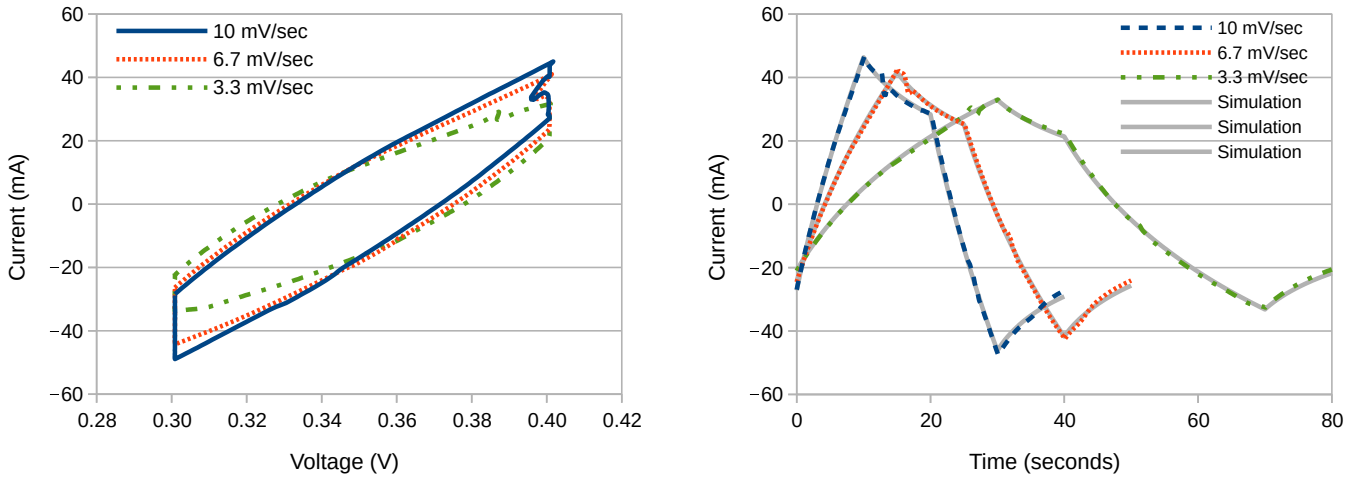

(**a**) Cyclic voltammograms

(**b**) Rearranged as transient waveforms

Figure 5. Cyclic Voltammetry measurements for Raney2 at three different voltage sweep rates. (**a**) Plotted as conventional voltammograms, and (**b**) plotted as a function of time. The best-fit RQ network simulations have been underlaid under the transient waveforms.

The results in Tables 1 and 3 show a consistent pattern, that being that the reported capacitance was greatest when the electrode was driven at the greatest EIS amplitude, or the fastest CV ramp-rate. The reason for this is not known, but it is perhaps significant that for CV the CPE phase-angle n fell to 0.67 at the fastest ramp-rate, and likewise for EIS the phase-angle fell to 0.60 at the largest amplitude. This is not within the normal valid range for the phase angle of a CPE, which is typically between 0.7 and 1.0. Instead, it is closer to the value of 0.5 that would be expected of a Warburg diffusion element. This may be an indication that the large electrode surface area and large amplitude or ramp-rate are impinging upon the mass-transportation limits of the electrolyte. Alternatively, it could be a sign that the assumptions on which Equation (3) is based were no longer valid. According to Brug et al. these assumptions are based on the observation of similar constant-phase behaviour in dielectric materials.

Given this pattern of results, it would therefore appear that the most accurate value for the roughness factor for Raney2 from Table 3 is that for the slowest ramp-rate, i.e., 42,490. This is many times larger than the figure of up to 1700 that was obtained by Marozzi et al. [15], the value of 3620 obtained by Ganesh et al. [46], and the figure of 4400 obtained by Suffredini et al. [47], all for electrodeposited forms of nickel onto metallic sheet. It is also larger than that measured for Raney nickel by Herraiz-Cardona et al., which was about 28,000 at zero HER over-potential [21].

EIS results for the same electrode confirm that the series resistance between WE and RE was 9.67 $\Omega\,cm^2$, which is close to the figure of 9.62 $\Omega\,cm^2$ produced by RQ Transient Best-fit, and builds confidence that this method is able to perform accurate measurements. Similarly, the value for the phase argument n of 0.70 is close to the value of 0.68 measured by EIS in Table 1 for a closely related coating. The average of the capacitance measurements was 1.89 $F\,cm^{-2}$, which equates to a roughness factor of 47,150, and helps to explain how the coating generated such impressively low overpotential figures. However, the value for the capacitance could not be confirmed by EIS, because the frequency range did not go low enough to reveal the point where the impedance magnitude increased. Nevertheless, in combination with Table 1, the CV measurement provides good evidence of the electrode's high surface area.

To further evaluate this high capacitance, a freshly deposited Raney2-coated electrode was investigated using cyclic-voltammetry over a wide voltage range, with the results as presented in Figure 6.

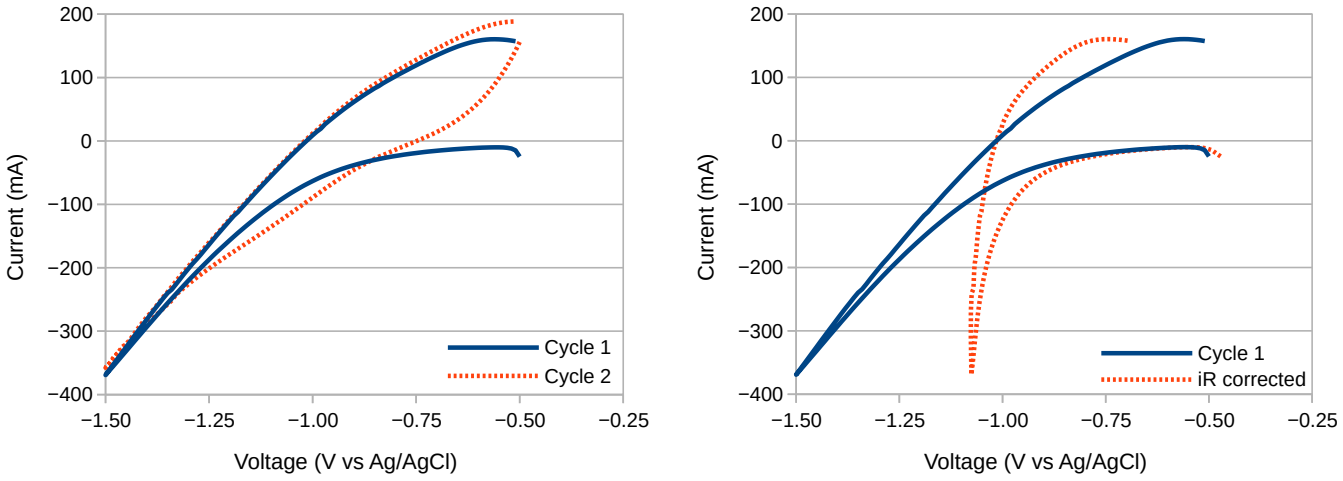

(**a**) Cyclic voltammetry (**b**) First cycle with iR-correction

Figure 6. Cyclic voltammetry starting at −0.5 V of a Raney2 cathode, (**a**) without and (**b**) with iR-correction. All sections with negative voltage and positive current were due to capacitance and hydride formation. Sweep rate: 10 mV s^{-1}.

The figure shows that on the cathodic sweep of cycle 1 the current remained negative, and below −1.1 V the electrode was evolving hydrogen. However, on the anodic sweep the current went positive at −1 V, which means that the electrode was supplying electrical power. This continued until the voltage reached −0.75 V on cycle 2. Since power is equal to current times voltage, it is possible to calculate the total electrical power supplied by the electrode between these two points. However, the voltage must be corrected for iR losses, as shown in Figure 6b, for which it is helpful to refer to the schematic diagram shown in Figure 7a.

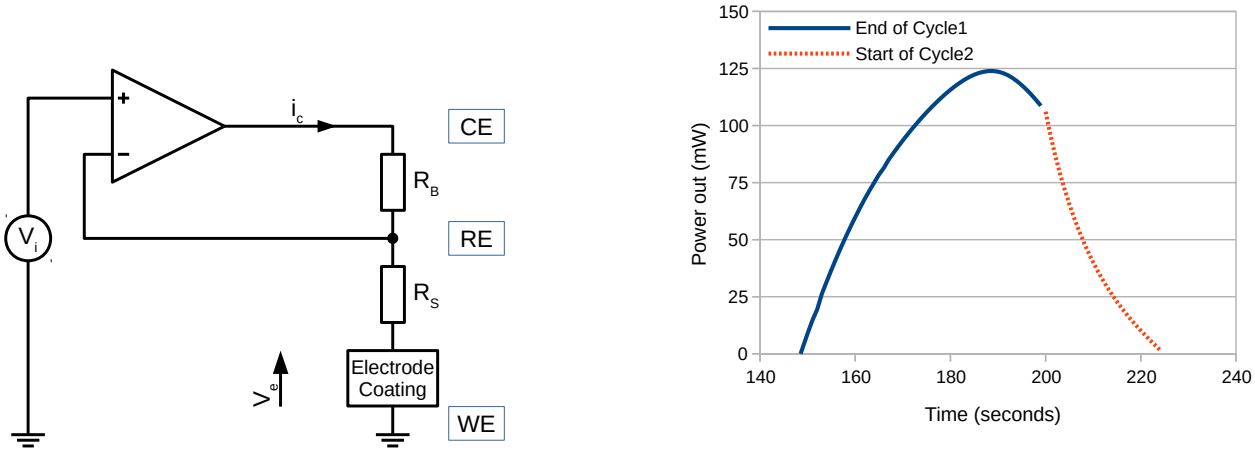

(**a**) Schematic diagram of potentiostat (**b**) Power out from electrode coating

Figure 7. Schematic diagram of potentiostat.

The potentiostat is represented by an amplifier, which continually alters the voltage of CE until the difference between RE and WE is equal to the desired input voltage V_i. No current passes into the negative input of the amplifier since it is high impedance.

The ohmic resistance of the electrolyte solution and electrical wiring, R_s, between RE and WE is known from EIS, based on the valid assumption that the electrode coating is a short-circuit at high-frequency. Regardless of the sign of i_c, this permits V_e to be calculated as:

$$V_e = V_i - i_c R_s \tag{9}$$

which is the equation for standard iR correction. Note that if i_c is of opposite polarity to V_i, then V_e will be *larger* than V_i. If at any time V_e and i_c are of opposite polarity, this means that the electrode coating is supplying electrical power, and the total energy out can be calculated by integrating the product of the two:

$$E_{e,out} = -\int V_e(t) i_c(t) dt \tag{10}$$

which is equivalent to measuring the area under the curve in Figure 7b. When this is done, the figure for the amount of energy released after one cycle is 5.5 J, which means that the Raney2 coating was able to store and release 0.61 J cm^{-2} in the form of hydride in a comparatively short period of time. Note that it is not possible to determine the ratio between energy stored and released, because some of the energy was used to split water.

4. Comparisons

Hydrogen evolution: A limited survey of recently published results for earth-abundant hydrogen evolution catalysts is as presented in Table 4. (Abbreviations: CC: carbon cloth; CCH: cobaltous carbonate hydroxide; CFP: carbon fibre paper; CNT: carbon nanotubes; DO: derived oxide; FTO: fluorine-doped tin oxide; GCE: glassy carbon electrode; LDH: layered double hydroxide; MNA: mesoporous nanorod array; MS: microsphere; NA: nanorod array; NF: nickel foam; NP: nanoplates; NR: nanorods; NrGO: nitrogenated reduced graphene oxide; NSh: nanosheets; Nst: nanostructures; NA: nanowire arrays). The table shows that the overpotential, at least at 10 mA cm^{-2}, can be almost arbitrarily small. As a result, some authors only quote the overpotential at 100 mA cm^{-2}, by which point hydrogen evolution is very well established. Therefore, the table has been generated by taking measurements from published diagrams, so as to establish a common baseline. Many papers also cite a well-known commercial catalyst called 'PtC' (platinum on carbon) as a baseline for comparison, therefore it has been included in the table, even though it is not earth-abundant. It is heartening to note that many of the catalysts are able to outperform it, including the Raney2 catalyst studied in this paper.

Table 4. Recent achievements in earth-abundant hydrogen evolution catalysis. All overpotentials quoted at 10 mA cm^{-2}. Catalyst PtC is noble-metal, and included for comparison purposes only.

Lead Author(s)	Year	Catalyst	Substrate	Electrolyte	Tafel Slope mV dec^{-1}	Overpotential mV
Wang Mingyong [48]	2015	NiMo	Cu	10 wt% NaOH	137	7
Wang Yuhang [49]	2014	3D NiMo	Cu foam	1 M NaOH		11
Song Fuzhang [50]	2018	Ni_3N/Ni	NF	1 M KOH		12
C Panda [51]	2019	$NiPt_3$@NiS	NF	1 M KOH	24	12
Yu Fang [52]	2018	FeP/Ni_2P	NF	1 M KOH	24.2	14
Zhang Jian [53]	2017	$MoNi_4/MoO_2$	NF	1 M KOH	30	15
Zhang Tao [54]	2018	Ni_5P_4@$NiCo_2O_4$	NF	1 M KOH	27	27
W. Gannon [37]	2019	Raney2	316SS	1 M KOH	50	28
R. Solmaz [28]	2017	NiZn-Au	Cu/Ni	1 M KOH	66	31
Men Yana [55]	2019	Ni−Co_2P	CC	1 M KOH	51	34
Chen Weiwu [56]	2019	S-NiP	NF	1 M KOH	44	35
Herraiz-Cardona [57]	2012	Ni	Cu foam	30 wt% KOH	103	41
Huang Yichao [58]	2019	1T-MoS_2	CFP	1 M KOH	52	43
Xiang Rui [59]	2019	PtC	NF	1 M KOH	53	46
Xiang Rui [59]	2019	Co@$CoMoO_4$	NF	1 M KOH	85	46
Gao M. [60]	2017	Ni-Mo MS	Cu	1 M KOH	49	49
Liu Caichi [61]	2020	Ni_2P−$NiSe_2$	CC	1 M KOH	72.6	66
Shi Zhangping [62]	2016	nano MoC	GCE	1 M KOH	50	77
Zhu Yanping [63]	2019	$CoSe_{1.26}P_{1.42}$	CC	1 M KOH	90	92
Xing Zhicai [64]	2016	Ni_3N	NF	1 M KOH	109	121
Lai Feili [65]	2019	Fe−$NiCo_2O_4$@HNCP	GCE	1 M KOH	47	124
Zhu Wenxin [66]	2016	NiS−MS	Ni foam	1 M KOH	83	134
Farjana Haque [67]	2019	2D Crys-AMO	NF	0.1 M KOH	50	138
Feng Yi [68]	2016	Ni-Co-P-300	not known	1 M KOH	61	150
Liang Hai-Wei [69]	2015	CoNx	C	1 M KOH	75	170

Oxygen evolution: A limited survey of recently published results for earth-abundant oxygen evolution catalysts is as presented in Table 5.

Table 5. Recent achievements in earth-abundant oxygen evolution catalysis. All overpotentials quoted at 10 mA cm^{-2}.

Lead Author(s)	Year	Catalyst	Substrate	Electrolyte	Tafel Slope mV dec^{-1}	Overpotential mV
Yu Fang [52]	2018	FeP/Ni_2P	NF	1 M KOH	22.7	154
Gao Chen [70]	2019	Amorphous LaNiFe	NF	1 M KOH	36	189
Bo Zhang [71]	2016	Gelled FeCoW	Au-plated NF	1 M KOH		191
Xiang Xu [72]	2016	$Ni_xFe_{1-x}Se_2$−DO	NF	1 M KOH	28	195
Lu Xunyu, Zhao Chuan [73]	2015	NiFe NSh	NF	1 M KOH	28	215
Chi Jun [74]	2018	FeOOH/NiFe	CCH NA	1 M KOH		220
Feng Yan [75]	2017	NiFe-N NSh	CC	1 M KOH	26	224
Liu Rong [76]	2017	CoFe LDH NSh	NF	1 M KOH	36	232
Nai Jianwei [77]	2017	Ni-Fe-Se disks	GCE	1 M KOH	26	240
Lu Xue Feng [78]	2017	$CoFe_2O_4$/C NRA	NF	1 M KOH	45	240
Wang Zhaoyang [79]	2016	NiFeSe NSh	CC	1 M KOH	47	229
Gong Ming [80]	2013	NiFe-LDH	CNT	1 M KOH	31	247
Lu Zhiyi [81]	2014	NiFe-LDH NP	Nickel	1 M KOH	43	250
Zhang Huabin [82]	2019	FeCoP nanoboxes	CFP	1 M KOH	31	269
Rodney Smith [83]	2013	$Fe_{40\%}Ni_{60\%}$	FTO	0.1 M KOH	34	284
Xu You [84]	2017	Ni@NC-800	NF	1 M KOH	45	285
Sengeni Anantharaj [85]	2017	CoP NSt	GC	1 M KOH	70	287
Yun-Pei Zhu [86]	2015	CoP-MNA	NF	1 M KOH	65	290
W. Gannon [37]	2019	Raney2	316SS	1 M KOH	38	293
Wang Huaping [87]	2019	LaFex$Ni_{1-x}O_3$ NR	GCE	1 M KOH	50	302
Zhang Huabin [88]	2019	HCM@Ni-N	Carbon	1 M KOH	76	304
Song Fang, Xile Hu [89]	2014	CoMn LDH	GC	1 M KOH	43	324
Guang Liu [90]	2016	$NiFe_2O_4$ NR	GC	1 M KOH	44	342
Santosh Bikkarolla [91]	2015	$CuCo_2O_4$	NrGO	1 M KOH	64	360
Jing Jiang [92]	2014	NiCo-LDH NSh	NF	0.1 M KOH	113	420

Although it can be difficult to make direct comparisons between catalysts, a picture has been emerging over recent years of the limits to which transition metals can be taken. At present this looks to be an overpotential of about 200 mV at a current density of 10 mA cm^{-2}. This current density is chosen because it is the most widely quoted figure, and because it is described as the most significant for solar fuel synthesis [40]. However, it is not the most significant figure for a commercial electrolyser, which benefits from attaining figures about two orders of magnitude higher. As an illustration of what is possible, figures of 690 mA cm^{-2} at an overpotential of 281 mV are quoted for the FeP/Ni_2P catalyst, whereas the NiFe-N catalyst has achieved 360 mA cm^{-2} at an overpotential of 255 mV, fully 220 mV less than the equivalent figure measured for IrO_2.

The table shows that the Raney2 catalyst is certainly not exceptional, being about 100 mV behind the leading edge. However, it is unusual in being one of only two bifunctional catalysts listed in the table. It should also be noted that the developers of the leading catalyst, FeCoW, discovered that any annealing of their catalyst had a destructive effect on its catalytic ability. This they ascribed to the phase separation of the ternary catalyst into discrete crystalline particles of Fe_3O_4, Co_3O_4 and $CoWO_4$. This therefore highlights the difficulty of producing highly active catalysts that are not subsequently prone to some form of instability.

As a bifunctional catalyst the Raney2 coating is not just highly stable, but also achieves a combined overpotential of just 320 mV at 10 mA cm^{-2}. In addition, since 10 of the higher-performing catalysts in Table 5 feature nickel or nickel-iron, the scope for increasing its specificity for OER appears promising.

5. Conclusions

This paper presents a new technique for the fitting of a resistor/constant-phase-element network to cyclic voltammetry (CV) waveforms recorded at open-circuit potential. From this a figure for the double-layer capacitance can be calculated, in accordance with Equation (3). The agreement between simulation and measurement is convincingly close, as shown in Figures 3b and 5b. As such the technique may help with the interpretation of CV results, especially ones involving very high capacitance where alternative techniques become problematic. In addition, there is no reason the technique cannot be extended to the fitting of an RQR network, including a charge transfer resistance, to waveforms recorded away from OCP.

This fitting technique permitted a value to be measured for the roughness factor of 42,500, which is larger than any comparable figures so far discovered in the literature. The coating also demonstrated potentially useful levels of performance as a supercapacitor material, where it attained a capacitance of 1.7 F cm^{-2}, and as a hydride storage material, where it stored 0.61 J cm^{-2}. However, possibly its greatest utility is as an electrocatalyst for water-splitting, both for hydrogen and oxygen evolution, where it achieved a combined overpotential of just 320 mV at the most widely reported benchmark figure of 10 mA cm^{-2}. This equates to a water-splitting voltage of just 1.55 V, and is just 70 mV above the thermoneutral voltage. Taking into consideration the simplicity of the deposition procedure, we believe this makes Raney2 the highest performing simple bifunctional electrocatalytic coating known.

Author Contributions: Conceptualization, C.W.D.; methodology, W.J.F.G.; software, W.J.F.G.; formal analysis, W.J.F.G.; investigation, W.J.F.G.; supervision, C.W.D.; funding acquisition, C.W.D. All authors have read and agreed to the published version of the manuscript.

Funding: This research received no external funding.

Institutional Review Board Statement: Not applicable.

Informed Consent Statement: Not applicable.

Data Availability Statement: The data presented in this study are openly available in FigShare at doi.org/10.6084/m9.figshare.13498692.

Acknowledgments: W.J.F.G. was funded by a College of Engineering Zienkiewicz PhD Scholarship from Swansea University, UK.

Conflicts of Interest: The authors declare no conflict of interest.

Abbreviations

The following abbreviations are used in this manuscript:

316SS	316-grade Stainless Steel
CE	Counter Electrode
CPE	Constant Phase Element
CV	Cyclic Voltammetry
EIS	Electrochemical Impedance Spectroscopy
HER	Hydrogen Evolution Reaction
ICT	Information and Communications Technology
OCP	Open-Circuit Potential
OER	Oxygen Evolution Reaction
PEM	Proton Exchange Membrane
RC	a Resistor–Capacitor network
RCR	a Resistor–Capacitor–Resistor network
RE	Reference Electrode
RQ	a Resistor–CPE(Q) network
SI	Supplementary Information
WE	Working Electrode

References

1. Jones, N. The Information Factories. *Nat. Mag.* **2018**, *561*, 163–166. [CrossRef] [PubMed]
2. Andrae, A.; Edler, T. On Global Electricity Usage of Communication Technology: Trends to 2030. *Challenges* **2015**, *6*, 117–157. [CrossRef]
3. Gannon, W.J.; Jones, D.R.; Dunnill, C.W. Enhanced Lifetime Cathode for Alkaline Electrolysis Using Standard Commercial Titanium Nitride Coatings. *Processes* **2019**, *7*, 112. [CrossRef]
4. Jones, D.; Phillips, R.; Gannon, W.J.; Rome, B.; Warwick, M.; Dunnill, C. Photocapacitive CdS/WOx nanostructures for solar energy storage. *Sci. Rep.* **2019**, *9*. [CrossRef] [PubMed]
5. Gannon, W.J.; Warwick, M.E.A.; Dunnill, C.W. Woven Stainless-Steel Mesh as a Gas Separation Membrane for Alkaline Water-Splitting Electrolysis. *Membranes* **2020**, *10*, 109. [CrossRef]
6. Yu, F.; Yu, L.; Mishra, I.K.; Yu, Y.; Ren, Z.F.; Zhou, H.Q. Recent developments in earth-abundant and non-noble electrocatalysts for water electrolysis. *Mater. Today Phys.* **2018**, *7*, 121–138. [CrossRef]
7. Medford, A.J.; Vojvodic, A.; Hummelshøj, J.S.; Voss, J.; Abild-Pedersen, F.; Studt, F.; Bligaard, T.; Nilsson, A.; Nørskov, J.K. From the Sabatier principle to a predictive theory of transition-metal heterogeneous catalysis. *J. Catal.* **2015**, *328*, 36–42. [CrossRef]
8. Eftekhari, A. Electrocatalysts for hydrogen evolution reaction. *Int. J. Hydrogen Energy* **2017**, *42*, 11053–11077. [CrossRef]
9. Nørskov, J.K.; Bligaard, T.; Logadottir, A.; Kitchin, J.R.; Chen, J.G.; Pandelov, S.; Stimming, U. Trends in the Exchange Current for Hydrogen Evolution. *J. Electrochem. Soc.* **2005**, *152*, J23. [CrossRef]
10. Smith, A.J.; Trimm, D.L. The Preparation of Skeletal Catalysts. *Annu. Rev. Mater. Res.* **2005**, *35*, 127–142. [CrossRef]
11. Schiller, G.; Henne, R.; Mohr, P.; Peinecke, V. High Performance Electrodes for an Advanced Intermittently Operated 10-kW Alkaline Water Electrolyzer. *Int. J. Hydrogen Energy* **1998**, *23*, 761–765. [CrossRef]
12. Endoh, E.; Otouma, H.; Morimoto, T.; Oda, Y. New Raney nickel composite-coated electrode for hydrogen evolution. *Int. J. Hydrogen Energy* **1987**, *12*, 473–479. [CrossRef]
13. Balej, J.; Divisek, J.; Schmitz, H.; Mergel, J. Preparation and properties of raney nickel electrodes on Ni-Zn base for H_2 and O2 evolution from alkaline solutions Part I: Electrodeposition of Ni-Zn alloys from chloride solutions. *J. Appl. Electrochem.* **1992**, *22*, 705–710. [CrossRef]
14. De Giz, M.J.; Machado, S.A.S.; Avaca, L.A.; Gonzalez, E.R. High area Ni-Zn and Ni-Co-Zn codeposits as hydrogen electrodes in alkaline solutions. *J. Appl. Electrochem.* **1992**, *22*, 973–977. [CrossRef]
15. Marozzi, C.A.; Chialvo, A.C. Development of electrode morphologies of interest in electrocatalysis. Part 1: Electrodeposited porous nickel electrodes. *Electrochim. Acta* **2000**, *45*, 2111–2120. [CrossRef]
16. Birry, L.; Lasia, A. Studies of the hydrogen evolution reaction on Raney nickel–molybdenum electrodes. *J. Appl. Electrochem.* **2004**, *34*, 735–749. [CrossRef]
17. Chade, D.; Berlouis, L.; Infield, D.; Cruden, A.; Nielsen, P.T.; Mathiesen, T. Evaluation of Raney nickel electrodes prepared by atmospheric plasma spraying for alkaline water electrolysers. *Int. J. Hydrogen Energy* **2013**, *38*, 14380–14390. [CrossRef]
18. Divisek, J.; Malinowski, P.; Mergel, J.; Schmitz, H. Improved components for advanced alkaline water electrolysis. *Int. J. Hydrogen Energy* **1988**, *13*, 141–150. [CrossRef]
19. Sheela, G.; Pushpavanam, M.; Pushpavanam, S. Zinc-nickel alloy electrodeposits for water electrolysis. *Int. J. Hydrogen Energy* **2002**, *27*, 627–633. [CrossRef]
20. Herraiz-Cardona, I.; Ortega, E.; Vázquez-Gómez, L.; Pérez-Herranz, V. Electrochemical characterization of a NiCo/Zn cathode for hydrogen generation. *Int. J. Hydrogen Energy* **2011**, *36*, 11578–11587. [CrossRef]
21. Herraiz-Cardona, I.; Ortega, E.; Pérez-Herranz, V. Impedance study of hydrogen evolution on Ni/Zn and Ni-Co/Zn stainless steel based electrodeposits. *Electrochim. Acta* **2011**, *56*, 1308–1315. [CrossRef]
22. Herraiz-Cardona, I.; González-Buch, C.; Valero-Vidal, C.; Ortega, E.; Pérez-Herranz, V. Co-modification of Ni-based type Raney electrodeposits for hydrogen evolution reaction in alkaline media. *J. Power Sources* **2013**, *240*, 698–704. [CrossRef]
23. González-Buch, C.; Herraiz-Cardona, I.; Ortega, E.; García-Antón, J.; Pérez-Herranz, V. Synthesis and characterization of macroporous Ni, Co and Ni-Co electrocatalytic deposits for hydrogen evolution reaction in alkaline media. *Int. J. Hydrogen Energy* **2013**, *38*, 10157–10169. [CrossRef]
24. Solmaz, R.; Döner, A.; Kardaş, G. Preparation, characterization and application of alkaline leached CuNiZn ternary coatings for long-term electrolysis in alkaline solution. *Int. J. Hydrogen Energy* **2010**, *35*, 10045–10049. [CrossRef]
25. Solmaz, R. Electrochemical preparation, characterization, and application of a novel cathode material, mild Steel/Ni/NiZn-Pt, for alkaline water electrolysis. *Energy Sources Part A: Recover. Util. Environ. Eff.* **2014**, *36*, 1212–1218. [CrossRef]
26. Solmaz, R.; Döner, A.; Doğrubaş, M.; Erdoğan, I.Y.; Kardaş, G. Enhancement of electrochemical activity of Raney-type NiZn coatings by modifying with PtRu binary deposits: Application for alkaline water electrolysis. *Int. J. Hydrogen Energy* **2016**, *41*, 1432–1440. [CrossRef]
27. Solmaz, R.; Salcı, A.; Yüksel, H.; Doğrubaş, M.; Kardaş, G. Preparation and characterization of Pd-modified Raney-type NiZn coatings and their application for alkaline water electrolysis. *Int. J. Hydrogen Energy* **2017**, *42*, 2464–2475. [CrossRef]
28. Solmaz, R. Gold-supported activated NiZn coatings: Hydrogen evolution and corrosion studies. *Int. J. Energy Res.* **2017**, *41*, 1452–1459. [CrossRef]
29. Balej, J. Electrocatalysts for oxygen evolution in advanced water electrolysis. *Int. J. Hydrogen Energy* **1985**, *10*, 89–99. [CrossRef]

30. Bates, M.K.; Jia, Q.; Doan, H.; Liang, W.; Mukerjee, S. Charge-Transfer Effects in Ni-Fe and Ni-Fe-Co Mixed-Metal Oxides for the Alkaline Oxygen Evolution Reaction. *ACS Catal.* **2016**, *6*, 155–161. [CrossRef]
31. Tsay, P.; Hu, C.C. Non-Anomalous Codeposition of Iron-Nickel Alloys Using Pulse-Reverse Electroplating Through Means of Experimental Strategies. *J. Electrochem. Soc.* **2002**, *149*, C492. [CrossRef]
32. Tozar, A.; Karahan, I.H. Structural and corrosion protection properties of electrochemically deposited nano-sized Zn-Ni alloy coatings. *Appl. Surf. Sci.* **2014**, *318*, 15–23. [CrossRef]
33. Soares, D.M. Hydride Effect on the Kinetics of the Hydrogen Evolution Reaction on Nickel Cathodes in Alkaline Media. *J. Electrochem. Soc.* **1992**, *139*, 98. [CrossRef]
34. Olivares-Ramírez, J.M.; Campos-Cornelio, M.L.; Godínez, J.U.; Borja-Arco, E.; Castellanos, R.H. Studies on the hydrogen evolution reaction on different stainless steels. *Int. J. Hydrogen Energy* **2007**, *32*, 3170–3173. [CrossRef]
35. Sapountzi, F.M.; Gracia, J.M.; Weststrate, C.K.J.; Fredriksson, H.O.; Niemantsverdriet, J.H. Electrocatalysts for the generation of hydrogen, oxygen and synthesis gas. *Prog. Energy Combust. Sci.* **2017**, *58*, 1–35. [CrossRef]
36. Divisek, J.; Schmitz, H.; Steffen, B. Electrocatalyst Materials Evolution for Hydrogen. *Electrochim. Acta* **1994**, *39*, 1723–1731. [CrossRef]
37. Gannon, W.J.; Dunnill, C.W. Raney Nickel 2.0: Development of a high-performance bifunctional electrocatalyst. *Electrochim. Acta* **2019**, *322*, 134687. [CrossRef]
38. Brug, G.J.; van den Eeden, A.L.G.; Sluyters-Rehbach, M.; Sluyters, J.H. The analysis of electrode impedances complicated by the presence of a constant phase element. *J. Electroanal. Chem.* **1984**, *176*, 275–295. [CrossRef]
39. Jovic, V. *Determination of the Correct Value of Cdl From the Impedance Results Fitted by the Commercially Available Software*; Technical Report; University of Belgrade, Belgrade, Serbia, 2003.
40. McCrory, C.C.L.; Jung, S.; Ferrer, I.M.; Chatman, S.M.; Peters, J.C.; Jaramillo, T.F. Benchmarking Hydrogen Evolving Reaction and Oxygen Evolving Reaction Electrocatalysts for Solar Water Splitting Devices. *J. Am. Chem. Soc.* **2015**, *137*, 4347–4357. [CrossRef]
41. Athanasiou, V.; Konkoli, Z. On the efficient simulation of electrical circuits with constant phase elements: The Warburg element as a test case. *Int. J. Circuit Theory Appl.* **2018**, *46*, 1072–1090. [CrossRef]
42. Gannon, W.J.; Dunnill, C.W. Apparent disagreement between cyclic voltammetry and electrochemical impedance spectroscopy explained by time-domain simulation of constant phase elements. *Int. J. Hydrogen Energy* **2020**, *45*, 22383–22393. [CrossRef]
43. Colli, A.N.; Girault, H.H.; Battistel, A. Non-precious electrodes for practical alkaline water electrolysis. *Materials* **2019**, *12*, 1–17. [CrossRef]
44. McCrory, C.C.L.; Jung, S.; Peters, J.C.; Jaramillo, T.F. Benchmarking heterogeneous electrocatalysts for the oxygen evolution reaction. *J. Am. Chem. Soc.* **2013**, *135*, 16977–16987. [CrossRef] [PubMed]
45. Bagotzky, V.S.; Khrushcheva, E.I.; Tarasevich, M.R.; Shumilova, N.A. Corrosion of platinum catalyst in alkaline solutions. *J. Power Sources* **1982**, *8*, 301–309. [CrossRef]
46. Ganesh, V.; Lakshminarayanan, V. Preparation of high surface area nickel electrodeposit using a liquid crystal template technique. *Electrochim. Acta* **2004**, *49*, 3561–3572. [CrossRef]
47. Suffredini, H.B.; Cerne, J.L.; Crnkovic, F.C.; MacHado, S.A.S.; Avaca, L.A. Recent developments in electrode materials for water electrolysis. *Int. J. Hydrogen Energy* **2000**, *25*, 415–423. [CrossRef]
48. Wang, M.; Wang, Z.; Yu, X.; Guo, Z. Facile one-step electrodeposition preparation of porous NiMo film as electrocatalyst for hydrogen evolution reaction. *Int. J. Hydrogen Energy* **2015**, *40*, 2173–2181. [CrossRef]
49. Wang, Y.; Zhang, G.; Xu, W.; Wan, P.; Lu, Z.; Li, Y.; Sun, X. A 3D Nanoporous Ni-Mo Electrocatalyst with Negligible Overpotential for Alkaline Hydrogen Evolution. *ChemElectroChem* **2014**, *1*, 1138–1144. [CrossRef]
50. Song, F.; Li, W.; Yang, J.; Han, G.; Liao, P.; Sun, Y. Interfacing nickel nitride and nickel boosts both electrocatalytic hydrogen evolution and oxidation reactions. *Nat. Commun.* **2018**, *9*. [CrossRef]
51. Panda, C.; Menezes, P.W.; Yao, S.; Schmidt, J.; Walter, C.; Hausmann, J.N.; Driess, M. Boosting Electrocatalytic Hydrogen Evolution Activity with a NiPt3@NiS Heteronanostructure Evolved from a Molecular Nickel-Platinum Precursor. *J. Am. Chem. Soc.* **2019**, *141*, 13306–13310. [CrossRef]
52. Yu, F.; Zhou, H.; Huang, Y.; Sun, J.; Qin, F.; Bao, J.; Goddard, W.A.; Chen, S.; Ren, Z. High-performance bifunctional porous non-noble metal phosphide catalyst for overall water splitting. *Nat. Commun.* **2018**, *9*, 1–9. [CrossRef]
53. Zhang, J.; Wang, T.; Liu, P.; Liao, Z.; Liu, S.; Zhuang, X.; Chen, M.; Zschech, E.; Feng, X. Efficient hydrogen production on MoNi 4 electrocatalysts with fast water dissociation kinetics. *Nat. Commun.* **2017**, *8*, 1–8. [CrossRef]
54. Zhang, T.; Yang, K.; Wang, C.; Li, S.; Zhang, Q.; Chang, X.; Li, J.; Li, S.; Jia, S.; Wang, J.; et al. Nanometric Ni5P4 Clusters Nested on $NiCo_2O_4$ for Efficient Hydrogen Production via Alkaline Water Electrolysis. *Adv. Energy Mater.* **2018**, *8*, 2–7. [CrossRef]
55. Men, Y.; Li, P.; Zhou, J.; Cheng, G.; Chen, S.; Luo, W. Tailoring the Electronic Structure of Co2P by N Doping for Boosting Hydrogen Evolution Reaction at All pH Values. *ACS Catal.* **2019**, *9*, 3744–3752. [CrossRef]
56. Chen, W.; Mishra, I.K.; Qin, Z.; Yu, L.; Zhou, H.; Sun, J.; Zhang, F.; Chen, S.; Wenya, G.E.; Yu, Y.; et al. Nickel phosphide based hydrogen producing catalyst with low overpotential and stability at high current density. *Electrochim. Acta* **2019**, *299*, 756–761. [CrossRef]
57. Herraiz-Cardona, I.; Ortega, E.; Vázquez-Gómez, L.; Pérez-Herranz, V. Double-template fabrication of three-dimensional porous nickel electrodes for hydrogen evolution reaction. *Int. J. Hydrogen Energy* **2012**, *37*, 2147–2156. [CrossRef]

58. Huang, Y.; Sun, Y.; Zheng, X.; Aoki, T.; Pattengale, B.; Huang, J.; He, X.; Bian, W.; Younan, S.; Williams, N.; et al. Atomically engineering activation sites onto metallic 1T-MoS 2 catalysts for enhanced electrochemical hydrogen evolution. *Nat. Commun.* **2019**, *10*, 1–11. [CrossRef]
59. Xiang, R.; Duan, Y.; Peng, L.; Wang, Y.; Tong, C.; Zhang, L.; Wei, Z. Three-dimensional Core@Shell Co@CoMoO4 nanowire arrays as efficient alkaline hydrogen evolution electro-catalysts. *Appl. Catal. B: Environ.* **2019**, *246*, 41–49. [CrossRef]
60. Gao, M.Y.; Yang, C.; Zhang, Q.B.; Zeng, J.R.; Li, X.T.; Hua, Y.X.; Xu, C.Y.; Dong, P. Facile electrochemical preparation of self-supported porous Ni-Mo alloy microsphere films as efficient bifunctional electrocatalysts for water splitting. *J. Mater. Chem. A* **2017**, *5*, 5797–5805. [CrossRef]
61. Liu, C.; Gong, T.; Zhang, J.; Zheng, X.; Mao, J.; Liu, H.; Li, Y.; Hao, Q. Engineering Ni2P-NiSe2 heterostructure interface for highly efficient alkaline hydrogen evolution. *Appl. Catal. B Environ.* **2020**, *262*. [CrossRef]
62. Shi, Z.; Wang, Y.; Lin, H.; Zhang, H.; Shen, M.; Xie, S.; Zhang, Y.; Gao, Q.; Tang, Y. Porous nanoMoC@graphite shell derived from a MOFs-directed strategy: An efficient electrocatalyst for the hydrogen evolution reaction. *J. Mater. Chem. A* **2016**, *4*, 6006–6013. [CrossRef]
63. Zhu, Y.; Chen, H.C.; Hsu, C.S.; Lin, T.S.; Chang, C.J.; Chang, S.C.; Tsai, L.D.; Chen, H.M. Operando unraveling of the structural and chemical stability of P-substituted CoSe 2 electrocatalysts toward hydrogen and oxygen evolution reactions in alkaline electrolyte. *ACS Energy Lett.* **2019**, *4*, 987–994. [CrossRef]
64. Xing, Z.; Li, Q.; Wang, D.; Yang, X.; Sun, X. Self-supported nickel nitride as an efficient high-performance three-dimensional cathode for the alkaline hydrogen evolution reaction. *Electrochim. Acta* **2016**, *191*, 841–845. [CrossRef]
65. Lai, F.; Feng, J.; Ye, X.; Zong, W.; He, G.; Miao, Y.E.; Han, X.; Ling, X.Y.; Parkin, I.P.; Pan, B.; et al. Energy level engineering in transition-metal doped spinel-structured nanosheets for efficient overall water splitting. *J. Mater. Chem. A* **2019**, *7*, 827–833. [CrossRef]
66. Zhu, W.; Yue, X.; Zhang, W.; Yu, S.; Zhang, Y.; Wang, J.; Wang, J. Nickel sulfide microsphere film on Ni foam as an efficient bifunctional electrocatalyst for overall water splitting. *Chem. Commun.* **2016**, *52*, 1486–1489. [CrossRef] [PubMed]
67. Haque, F.; Zavabeti, A.; Zhang, B.Y.; Datta, R.S.; Yin, Y.; Yi, Z.; Wang, Y.; Mahmood, N.; Pillai, N.; Syed, N.; et al. Ordered intracrystalline pores in planar molybdenum oxide for enhanced alkaline hydrogen evolution. *J. Mater. Chem. A* **2019**, *7*, 257–268. [CrossRef]
68. Feng, Y.; Yu, X.Y.; Paik, U. Nickel cobalt phosphides quasi-hollow nanocubes as an efficient electrocatalyst for hydrogen evolution in alkaline solution. *Chem. Commun.* **2016**, *52*, 1633–1636. [CrossRef]
69. Liang, H.W.; Brüller, S.; Dong, R.; Zhang, J.; Feng, X.; Müllen, K. Molecular metal-Nx centres in porous carbon for electrocatalytic hydrogen evolution. *Nat. Commun.* **2015**, *6*, 1–8. [CrossRef]
70. Chen, G.; Zhu, Y.; Chen, H.M.; Hu, Z.; Hung, S.F.; Ma, N.; Dai, J.; Lin, H.J.; Chen, C.T.; Zhou, W.; et al. An Amorphous Nickel–Iron-Based Electrocatalyst with Unusual Local Structures for Ultrafast Oxygen Evolution Reaction. *Adv. Mater.* **2019**, *31*, 1–7. [CrossRef]
71. Zhang, B.; Zheng, X.; Voznyy, O.; Comin, R.; Bajdich, M.; Arquer, F.P.G.D.; Dinh, C.T.; Fan, F.; Yuan, M.; Janmohamed, A.; et al. Homogeneously dispersed multimetal oxygen-evolving catalysts. *Science* **2016**, *352*, 333–337. [CrossRef]
72. Xu, X.; Song, F.; Hu, X. A nickel iron diselenide-derived efficient oxygen-evolution catalyst. *Nat. Commun.* **2016**, *7*, 12324. [CrossRef] [PubMed]
73. Lu, X.; Zhao, C. Electrodeposition of hierarchically structured three-dimensional nickel–iron electrodes for efficient oxygen evolution at high current densities. *Nat. Commun.* **2015**, *6*, 1–7. [CrossRef] [PubMed]
74. Chi, J.; Yu, H.; Jiang, G.; Jia, J.; Qin, B.; Yi, B.; Shao, Z. Construction of orderly hierarchical FeOOH/NiFe layered double hydroxides supported on cobaltous carbonate hydroxide nanowire arrays for a highly efficient oxygen evolution reaction. *J. Mater. Chem. A* **2018**, *6*, 3397–3401. [CrossRef]
75. Yan, F.; Wang, Y.; Li, K.; Zhu, C.; Gao, P.; Li, C.; Zhang, X.; Chen, Y. Highly Stable Three-Dimensional Porous Nickel-Iron Nitride Nanosheets for Full Water Splitting at High Current Densities. *Chem. Eur. J.* **2017**. [CrossRef] [PubMed]
76. Liu, R.; Wang, Y.; Liu, D.; Zou, Y.; Wang, S. Water-Plasma-Enabled Exfoliation of Ultrathin Layered Double Hydroxide Nanosheets with Multivacancies for Water Oxidation. *Adv. Mater.* **2017**, *29*, 1–7. [CrossRef]
77. Nai, J.; Lu, Y.; Yu, L.; Wang, X.; Lou, X.W.D. Formation of Ni–Fe Mixed Diselenide Nanocages as a Superior Oxygen Evolution Electrocatalyst. *Adv. Mater.* **2017**, *29*, 1–8. [CrossRef] [PubMed]
78. Lu, X.F.; Gu, L.F.; Wang, J.W.; Wu, J.X.; Liao, P.Q.; Li, G.R. Bimetal-Organic Framework Derived $CoFe_2O_4$/C Porous Hybrid Nanorod Arrays as High-Performance Electrocatalysts for Oxygen Evolution Reaction. *Adv. Mater.* **2017**, *29*. [CrossRef]
79. Wang, Z.; Li, J.; Tian, X.; Wang, X.; Yu, Y.; Owusu, K.A.; He, L.; Mai, L. Porous Nickel-Iron Selenide Nanosheets as Highly Efficient Electrocatalysts for Oxygen Evolution Reaction. *ACS Appl. Mater. Interfaces* **2016**, *8*, 19386–19392. [CrossRef]
80. Gong, M.; Li, Y.; Wang, H.; Liang, Y.; Wu, J.Z.; Zhou, J.; Wang, J.; Regier, T.; Wei, F.; Dai, H. An Advanced Ni - Fe Layered Double Hydroxide Electrocatalyst for Water Oxidation. *J. Am. Chem. Soc.* **2013**, *135*, 8452–8455. [CrossRef]
81. Lu, Z.; Xu, W.; Zhu, W.; Yang, Q.; Lei, X.; Liu, J.; Li, Y.; Sun, X.; Duan, X. Three-dimensional NiFe layered double hydroxide film for high-efficiency oxygen evolution reaction. *Chem. Commun.* **2014**, *50*, 6479. [CrossRef]
82. Zhang, H.; Zhou, W.; Dong, J.; Lu, X.F.; Lou, X.W.D. Intramolecular electronic coupling in porous iron cobalt (oxy)phosphide nanoboxes enhances the electrocatalytic activity for oxygen evolution. *Energy Environ. Sci.* **2019**, *12*, 3348–3355. [CrossRef]

83. Smith, R.D.L.; Prévot, M.S.; Fagan, R.D.; Trudel, S.; Berlinguette, C.P. Water Oxidation Catalysis: Electrocatalytic Response to Metal Stoichiometry in Amorphous Metal Oxide Films Containing Iron, Cobalt, and Nickel. *J. Am. Chem. Soc.* **2013**, *135*, 11580–11586. [CrossRef] [PubMed]
84. Xu, Y.; Tu, W.; Zhang, B.; Yin, S.; Huang, Y.; Kraft, M.; Xu, R. Nickel Nanoparticles Encapsulated in Few-Layer Nitrogen-Doped Graphene Derived from Metal–Organic Frameworks as Efficient Bifunctional Electrocatalysts for Overall Water Splitting. *Adv. Mater.* **2017**, *29*, 1–8. [CrossRef] [PubMed]
85. Anantharaj, S.; Reddy, P.N.; Kundu, S. Core-Oxidized Amorphous Cobalt Phosphide Nanostructures: An Advanced and Highly Efficient Oxygen Evolution Catalyst. *Inorg. Chem.* **2017**, *56*, 1742–1756. [CrossRef] [PubMed]
86. Zhu, Y.P.; Liu, Y.P.; Ren, T.Z.; Yuan, Z.Y. Self-supported cobalt phosphide mesoporous nanorod arrays: A flexible and bifunctional electrode for highly active electrocatalytic water reduction and oxidation. *Adv. Funct. Mater.* **2015**, *25*, 7337–7347. [CrossRef]
87. Wang, H.; Wang, J.; Pi, Y.; Shao, Q.; Tan, Y.; Huang, X. Double Perovskite $LaFe_x$ Ni_{1-x} O 3 Nanorods Enable Efficient Oxygen Evolution Electrocatalysis. *Angew. Chem. Int. Ed.* **2019**, *58*, 2316–2320. [CrossRef]
88. Zhang, H.; Liu, Y.; Chen, T.; Zhang, J.; Zhang, J.; Lou, X.W. Unveiling the Activity Origin of Electrocatalytic Oxygen Evolution over Isolated Ni Atoms Supported on a N-Doped Carbon Matrix. *Adv. Mater.* **2019**, *31*, 1–7. [CrossRef]
89. Song, F.; Hu, X. Ultrathin Cobalt - Manganese Layered Double Hydroxide Is an Efficient Oxygen Evolution Catalyst. *J. Am. Chem. Soc.* **2014**, *136*, 16481–16484. [CrossRef]
90. Liu, G.; Wang, K.; Gao, X.; He, D.; Li, J. Fabrication of mesoporous $NiFe_2O_4$ nanorods as efficient oxygen evolution catalyst for water splitting. *Electrochim. Acta* **2016**, *211*, 871–878. [CrossRef]
91. Bikkarolla, S.K.; Papakonstantinou, P. CuCo2O4 nanoparticles on nitrogenated graphene as highly efficient oxygen evolution catalyst. *J. Power Sources* **2015**, *281*, 243–251. [CrossRef]
92. Jiang, J.; Zhang, A.; Li, L.; Ai, L. Nickel-cobalt layered double hydroxide nanosheets as high-performance electrocatalyst for oxygen evolution reaction. *J. Power Sources* **2015**, *278*, 445–451. [CrossRef]